The Journal of Chemical Physics | ARTICLE | scitation.org/journal/jcp

Spin–orbit coupling and vibronic transitions of Ce(C_3H_4) and Ce(C_3H_6) formed by the Ce reaction with propene: Mass-analyzed threshold ionization and relativistic quantum computation

Cite as: J. Chem. Phys. **152**, 144304 (2020); doi: 10.1063/5.0002505
Submitted: 25 January 2020 • Accepted: 23 March 2020 •
Published Online: 10 April 2020

Yuchen Zhang and Dong-Sheng Yang[a]

AFFILIATIONS

Department of Chemistry, University of Kentucky, Lexington, Kentucky 40506-0055, USA

[a] **Author to whom correspondence should be addressed:** dyang0@uky.edu

ABSTRACT

A Ce atom reaction with propene is carried out in a pulsed laser vaporization molecule beam source. Several Ce–hydrocarbon species formed by the C—H and C—C bond activation of propene are observed by time-of-flight mass spectrometry, and Ce(C_3H_n) (n = 4 and 6) are characterized by mass-analyzed threshold ionization (MATI) spectroscopy and density functional theory, multiconfiguration, and relativistic quantum chemical calculations. The MATI spectrum of each species consists of two vibronic band systems, each with several vibronic bands. Ce(C_3H_6) is identified as an inserted species with Ce inserting into an allylic C—H bond of propene and Ce(C_3H_4) as a metallocycle through 1,2-vinylic dehydrogenation. Both species have a C_s structure with the Ce $4f^1 6s^1$ ground valence electron configuration in the neutral molecule and the Ce $4f^1$ configuration in the singly charged ion. The two vibronic band systems observed for each species are attributed to the ionization of two pairs of the lowest spin–orbit coupled states with each pair being nearly degenerate.

I. INTRODUCTION

Spin–orbit coupling (SOC) relaxes the spin selection rules and makes it possible for transitions between electronic states of different spin multiplicities and for chemical reactions crossing different spin states. The phenomenon of the intersystem crossing in nonradiative transitions has a broad range of scientific and technological applications in materials sciences,[1–5] molecular photonics,[6] photosensitizer,[7] and photodynamic therapy.[8] Similarly, the spin-flipping along chemical reaction coordinates has important implications in molecular activations[9–15] and enzymatic reactions.[16] In addition to the relaxation of spin selection rules, SOC also affects the chemical bonding and molecular structures.[17–19]

Relativistic quantum chemical computations have been reported for numerous f-block-containing molecules.[20–49] In contrast, spectroscopic measurements of the SOC effect of the heavy-element containing molecules have considerably lagged behind. Such measurements are desirable because computations with various sophisticated models have not always produced consistent results,[17,18] and spectroscopic measurements could provide benchmarks for testing the accuracies of various computational models and possibly guide theoretical model improvements or new developments. We recently investigated the SOC effect of several reactive Ce-containing molecular species formed in the bond activation of small molecules and found that the extent of the spin-state mixing was affected not only by the atoms or groups that bind with the Ce atom but also by the shape of the molecules.[50–52] For example, the separation of the lowest-energy SOC levels of Ce(C_4H_6) is about 50% larger in a tetrahedron-like C_{3v} structure than in a cyclic C_s structure.[52]

As one of the simplest alkene molecules and the most important raw chemicals in the petroleum industry, metal-mediated propene reactions have received considerable attention in experimental chemical physics and physical chemistry communities. Its reactions with metal ions were mainly studied by Fourier-transform ion-cyclotron resonance, guided-ion-beam, or other mass-spectrometry based methods.[53–61] Its reactions with the neutral atoms were monitored by photoionization mass spectrometry of the resultant species or laser-induced fluorescence measurements of the depletion of the metal atom concentration.[62–69] Recently, we characterized reactive La–hydrocarbon species formed by dehydrogenation, metal insertion, and carbon–carbon bond cleavage and coupling using mass analyzed threshold ionization (MATI) spectroscopy and investigated reaction mechanisms in combination with density functional theoretical calculations.[70,71] In the reaction with propene, the La atom undergoes an electron promotion from the ground valence electron configuration $5d^1 6s^2$ to a low-energy configuration $5d^2 6s^1$ to facilitate the La–C bonding between the La $5d_\pi$ and propene C 2p orbitals, and the resultant La–hydrocarbon species all have the ground electron configuration $6s^1$. The Ce atom has the valence electron configuration $4f^1 5d^1 6s^2$ and is expected to have similar reactivity to the La atom because the compact 4f orbitals are not envisioned to significantly participate in chemical bonding. Thus, the resultant Ce–hydrocarbon species from the Ce-propene reaction are expected to have the ground electron configuration $4f^1 6s^1$, with the remaining two 5d electrons that are associated with the isolated Ce atom are spin paired with one or two ligand orbitals. The coupling of the 4f and $6s^1$ orbitals would yield seven triplets and seven singlets depending on the relative orientation of the $4f^1$ and $6s^1$ electrons. Furthermore, these triplets and singlets could interact with each other and result in dense low-energy states and potentially complex electronic spectra. This article reports the MATI spectroscopy and relativistic quantum chemical calculations of $Ce(C_3H_6)$ and $Ce(C_3H_4)$ formed in the Ce + propene reaction. The MATI spectroscopy is used to measure the possible SOC and vibronic transitions, and the quantum computations are used to characterize if the observed energy states arise from the mixing of the electronic states of different spins and if so, to what extent of such mixing is.

II. EXPERIMENTAL AND COMPUTATIONAL METHODS

A. Experimental

The metal-cluster beam instrument used in this work consists of reaction and spectroscopy vacuum chambers and was described in a previous publication.[72] $Ce(C_3H_4)$ and $Ce(C_3H_6)$ were formed by the Ce atom reaction with propene (99+ %, Aldrich) in a laser vaporization metal cluster beam source. Ce atoms were generated by pulsed-laser (Nd:YAG, Continuum Minilite II, 532 nm, ~2 mJ/pulse) vaporization of a Ce rod (99%, Metallium) in the presence of the propene/He mixture (~10^{-4}, 40 psi) delivered by a home-made piezoelectric pulsed valve. The metal atoms and gas mixture entered a collision tube (2 mm diameter and 2 cm length) and were then expanded into the reaction chamber, collimated by a cone-shaped skimmer (2 mm inner diameter), and passed through a pair of deflection plates. Ionic species in the molecular beam that were formed during laser vaporization were removed by an electric field (100 V cm^{-1}) applied on the deflection plates. The neutral products were identified by photoionization time-of-flight (TOF) mass spectrometry. A separate experiment was carried out to confirm that propene was activated by Ce rather than the vaporization laser. In this experiment, propene vapor was introduced 3 cm downstream of the laser vaporization point. The reaction products formed in the two experiments were identical, though a higher propene concentration in this experiment was required to produce comparable ion intensity in the mass spectra. Because propene bypassed the vaporization region, the direct excitation of the alkene compound via the vaporization laser plays no role in the hydrocarbon activation.

Prior to the MATI measurements, the photoionization efficiency spectra of $Ce(C_3H_6)$ and $Ce(C_3H_4)$ were recorded to locate their approximate ionization thresholds to guide MATI scans. In the MATI experiment, $Ce(C_3H_6)$ or $Ce(C_3H_4)$ was excited to high-lying Rydberg states in a single-photon process and ionized by a delayed pulsed electric field. The excitation laser was the same as that for photoionization in the mass spectrometric and photoionization efficiency experiments and was the frequency doubled output of a tunable dye laser (Lumonics HD-500), pumped by the third harmonic output (355 nm) of a Nd:YAG laser (Continuum Surelite II). The laser beam was collinear and counter propagating with the molecular beam. The ionization pulsed field (320 V cm^{-1}) was generated by using two high voltage pulse generators (DEI, PVX-4140) and delayed by 20 μs from the laser pulse by using a delayed pulsed generator (SRS, DG645). A small DC field (4.8 V cm^{-1}) was applied to separate the ions produced by direct photoionization from the MATI ions generated by delayed field ionization. The MATI ion signal was obtained by scanning the wavelength of the tunable dye laser, detected by using a dual microchannel plate detector, amplified by using a preamplifier (SRS, SR445), visualized by using a digital oscilloscope (Tektronix TDS 3012), and stored in a laboratory computer. Laser wavelengths were calibrated against vanadium atomic transitions in the MATI spectral region. The Stark shift on the ionization energy (IE) induced by the DC separation field was calculated using the relation $\Delta IE = 6.1E_f^{1/2}$, where E_f is in V cm^{-1} and ΔIE is in cm^{-1}.[73]

B. Computational

The density functional theory (DFT) method with Becke's three-parameter hybrid functional with the correlation functional of Lee, Yang, and Parr (B3LYP) was used to calculate the equilibrium geometries and vibrational frequencies of the neutral molecules and singly charged positive ions. The basis sets used in these calculations were 6-311+G(d, p) for C and H and the Stuttgart/Dresden (SDD) effective-core-potential basis set with 28 electron cores for Ce. No symmetry restrictions were imposed in initial geometry optimizations, but appropriate point groups were assigned in subsequent optimizations to help identify electronic symmetries. For each optimized stationary point, a vibrational analysis was performed to identify the nature of the stationary point (minimum or saddle point). The DFT calculations were performed with the Gaussian 09 software package.[74] To compare with the experimental MATI spectra, multidimensional Franck–Condon (FC) factors were calculated from the equilibrium geometries, harmonic vibrational frequencies, and normal coordinates of the neutral and ionized complexes.[75] In these calculations, recursion relations were employed and the Duschinsky effect was considered to account for a possible axis rotation from the neutral complex to the cation. Spectral simulations were performed using the experimental linewidth and Lorentzian line shape. Transitions from excited vibrational levels of the neutral molecule were considered by assuming thermal excitation at specific temperatures.

Relativistic quantum chemical computations were carried out to account for the observed two band systems in the MATI spectra. These calculations involved two steps: the first step included scalar relativity corrections in the self-consistent field (SCF) process and the second step the additional Breit–Pauli operator as a perturbation in the final SOC computations. Scalar relativity was incorporated into the calculations using the local unitary transformation approximation[76] for the infinite order two component transformations[77,78] of the one-electron integrals. The orbital bases used in these calculations were quadruple zeta-quality core-correlating all-electron basis sets of Noro and co-workers (QZC).[38,79] Since only *spdfg* basis sets could be used in the gradient calculations, the 3*h* and 1*i* functions in the standard QZC basis for Ce were truncated from all calculations, but the full QZC bases for C and H were retained. This basis set family has correlating functions for the valence and all upper core orbitals of Ce (as well as the 1*s* of C) so that the only orbitals excluded from correlation treatments were the deep core of Ce (1*s*, 2*sp*, and 3*spd* shells). The equation of motion coupled-cluster (EOM-CCSD) calculations[80] based on high-spin restricted open shell SCF (ROHF)[81] wavefunctions were used to survey the excited states of both neutral and cation. Because of computational limitations, these EOM-CCSD calculations employed the double zeta core correlating basis set (DZC).[38,79] SOC calculations were based on small configuration interaction calculations whose orbitals were obtained using the state-averaged multi-configuration self-consistent field (MCSCF) method.[82] In these MCSCF calculations, the active spaces were two electrons with eight molecular orbitals (2, 8) for the neutral radical and one electron with seven molecular orbitals (1,7) for the singly charged ion. These molecular orbitals were Ce-based 6s and 4f atomic orbitals with Ce $4f^1 6s^1$ electrons in the neutral species and 4f orbitals with a $4f^1$ electron in the ion. Dynamic correlation and SOC effects were treated as simultaneous perturbations by multi-reference quasi-degenerate perturbation theory (MCQDPT).[40,83] The SOC calculations used the full Breit–Pauli operator.[84,85] All relativistic calculations were performed using the GAMESS quantum chemistry package.[86]

III. RESULTS AND DISCUSSION

A. Ce + propene reaction

Figure 1 displays the TOF mass spectrum of the Ce reaction with propene recorded following photoionization at 239 nm. The mass spectrum shows mass peaks corresponding to $Ce(C_2H_2)$, $Ce(C_3H_n)$ (n = 4 and 6), $Ce(C_4H_6)$, and $Ce(C_6H_m)$ (m = 10 and 12). These complexes are formed through primary and secondary reactions. The primary reactions between Ce and propene (C_3H_6) yield $Ce(C_3H_6)$ through the association or metal insertion into one of the C—H bonds, $Ce(C_3H_4)$ through the dehydrogenation of $Ce(C_3H_6)$, and $Ce(C_2H_2)$ through the demethylation of $Ce(C_3H_6)$. Secondary reactions responsible for the formation of the other metal–hydrocarbon species are likely $Ce(C_3H_4) + C_3H_6 \rightarrow Ce(C_4H_6) + C_2H_4$, $Ce(C_3H_4) + C_3H_6 \rightarrow Ce(C_6H_{10})$, and $Ce(C_3H_6) + C_3H_6 \rightarrow Ce(C_6H_{12})$. In addition to the metal–hydrocarbon species, the mass spectrum shows the mass peaks corresponding to CeO and Ce, which are likely generated by two-photon ionization processes as their IEs are higher than the laser energy used for recording the TOF mass spectra.[36,87] CeO could be formed by the reaction of Ce atoms with oxygen present in the helium carrier gas as an impurity or by the laser vaporization of Ce oxide impurity in the Ce rod.[50–52] The metal–hydrocarbon species observed in the Ce + propene reaction are similar to those of the corresponding La reaction, with the exception of the C—C cleavage species.[70,71] The C—C cleavage produces $Ce(C_2H_2)$ through propene demethylation in the Ce reaction, whereas it yields $La(CH_2)$ by the removal of a C_2H_4 molecule from propene in the La reaction. The demethylation is likely the result of breaking the single C—C bond, while the removal of the C_2H_4 molecule could result from the breakage of the C=C double bond of a propene molecule. The observation of different C—C decoupling species reflects a subtle difference between Ce and La reactivities. In this article, we will focus on the spectroscopic and computational characterizations of two Ce radicals formed by the primary reactions: $Ce(C_3H_6)$ and $Ce(C_3H_4)$.

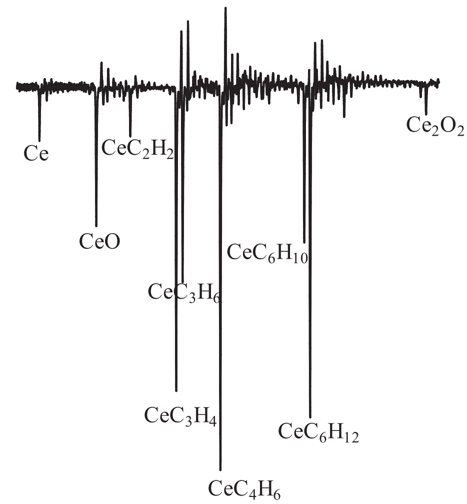

FIG. 1. TOF mass spectra of the molecular beams produced by the Ce atom reaction with propene recorded following photoionization at 239 nm. Seeding concentration of the organic compounds in He was ∼10^{-4}.

B. MATI spectra

The MATI spectrum of $Ce(C_3H_6)$ [Fig. 2(a)] consists of two band systems, each with two 272 cm^{-1} intervals above the respective origin band and a 240 cm^{-1} interval below. The origin bands of the two systems are located at 41 868 (10) cm^{-1} and 41 803 (10) cm^{-1}, respectively. For the higher energy band system, the spectrum also shows a weaker and less resolved band at 330 cm^{-1} above the origin band and a 32 cm^{-1} shoulder superimposed on the 272 cm^{-1} progression. The spectrum of $Ce(C_3H_4)$ [Fig. 3(a)] is observed at a slightly lower energy than that of $Ce(C_3H_6)$ and is congested above the two well-resolved bands at 41 035 (10) cm^{-1} and 40 909 (10) cm^{-1}. However, careful inspection shows that the observed transitions consist of well-structured vibrational bands. Associated with the strongest band at 41 035 cm^{-1} are vibrational intervals of 557 cm^{-1}, 440 cm^{-1}, and 205 cm^{-1}. Above the 40 909 cm^{-1} band,

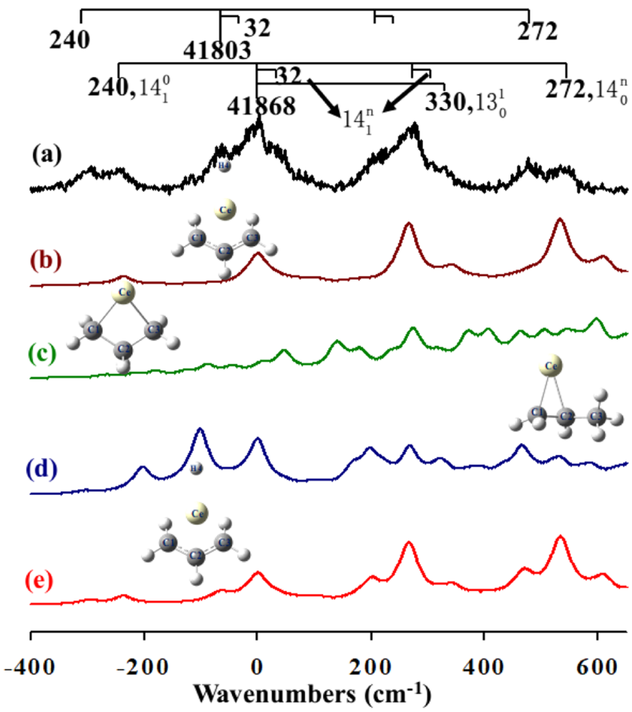

FIG. 2. MATI spectrum (a) and simulations of $Ce(C_3H_6)$ (b)–(e) at 200 K. Simulation is (b) for the $^2A' \leftarrow {}^3A'$ transition of $H{-}Ce(CH_2CHCH_2)$ (C_s), (c) for the $^2A' \leftarrow {}^3A'$ transition of $Ce(CH_2CH_2CH_2)$ (C_s), (d) for the $^2A \leftarrow {}^3A$ transition of $Ce(CH_2CHCH_3)$ (C_1), and (e) for the simulation representing the SOC $1^2E_{1/2} \leftarrow 1A'/2A'$ and $1^2E_{1/2} \leftarrow 1A''/2A''$ ($S \approx 1$) transitions of $H{-}Ce(CH_2CHCH_2)$. In the vibronic band assignments 14^n_1 and 14^n_0, n = 1 and 2.

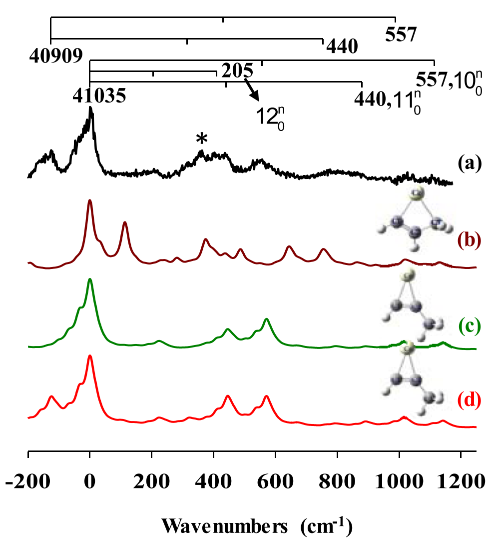

FIG. 3. MATI spectrum (a) and simulations of $Ce(C_3H_4)$ (b)–(d) at 200 K. Simulation is (b) for the $^2A \leftarrow {}^3A$ transition of $Ce(CHCHCH_2)$ (C_1), (c) for the $^2A' \leftarrow {}^3A'$ transition of $Ce(CHCCH_3)$ (C_s), and (d) for the simulation representing the SOC $1^2E_{1/2} \leftarrow 1A''/2A''$($S \approx 1$) and $1^2E_{1/2} \leftarrow 1A'/2A'$ transitions of $Ce(CHCCH_3)$. In the vibronic band assignments 10^n_0, 11^n_0, and 12^n_0, n = 1 and 2.

the 557 cm^{-1} and 440 cm^{-1} intervals can also be identified. Thus, the spectrum of $Ce(C_3H_4)$ also involves two band systems with the same (557 cm^{-1} and 440 cm^{-1}) vibrational progressions, though the weaker 205 cm^{-1} transition is not clearly shown in the 40 909 cm^{-1} band system. In addition to the above vibronic bands, the spectrum also shows a band at 360 cm^{-1} (marked with "*") to the blue of the 41 035 cm^{-1} band origin.

C. Structures and vibronic transitions without spin–orbit coupling

Figure 4 shows three low-energy isomers of $Ce(C_3H_6)$ [$H{-}Ce(CH_2CHCH_2)$, $Ce(CH_2CH_2CH_2)$, and $Ce(CH_2CHCH_3)$] and two isomers of $Ce(C_3H_4)$ [$Ce(CHCHCH_2)$ and $Ce(CHCCH_3)$], and Tables S1 and S2 give the bond lengths and angles of these isomers. The most stable isomer of $Ce(C_3H_6)$ is predicted to be an inserted species $H{-}Ce(CH_2CHCH_2)$ and identified as the carrier of the observed spectrum. The two isomers of $Ce(C_3H_4)$ lie close in energy, and the three-membered cyclic species $Ce(CHCCH_3)$ is identified as the spectral carrier. In analyzing the observed vibronic transitions, we first compare the measurements with DFT calculations and spectral simulations without involving SOC. Such comparisons indicate that only one of the two MATI band systems can be explained by the DFT calculations.

$Ce(C_3H_6)$: $Ce(C_3H_6)$ could be formed by Ce addition to propene or insertion into one of its C—H bonds. Our DFT/B3LYP calculations locate three isomers, as shown in Figs. 4(a)–4(c). The most stable isomer is an inserted species $H{-}Ce(CH_2CHCH_2)$ (C_s) with Ce insertion into an allylic C—H bond of the methyl group [Fig. 4(a)]. The insertion of the allylic C—H bond is preferred because it is weaker than a vinylic C—H bond. The second lowest-energy isomer is a four-membered cyclic complex $Ce(CH_2CH_2CH_2)$ (C_s) with Ce binding with two terminal carbon atoms [Fig. 4(b)], which is ~0.30 eV higher in energy than the inserted species. The

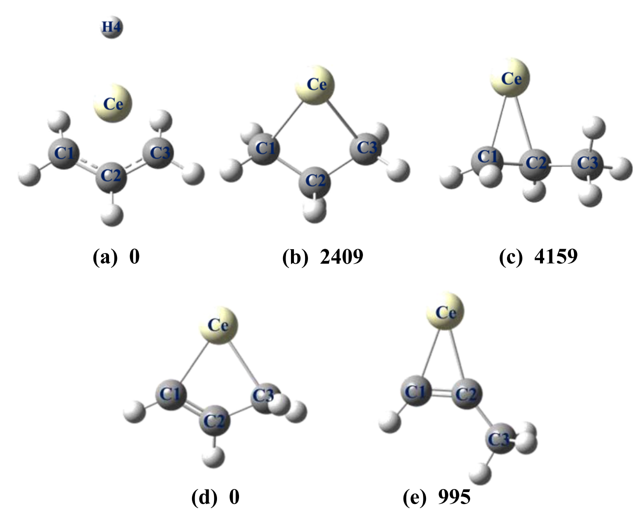

FIG. 4. Isomers and relative energies (cm^{-1}) of $Ce(C_3H_6)$ and $Ce(C_3H_4)$: (a) $H{-}Ce(CH_2CHCH_2)$ (C_s), (b) $Ce(CH_2CH_2CH_2)$ (C_s), (c) $Ce(CH_2CHCH_3)$ (C_1), (d) $Ce(CHCHCH_2)$ (C_1), and (e) $Ce(CHCCH_3)$ (C_s).

four-membered cycle is an association complex where one of the hydrogen atoms in the methyl group is migrated to the middle carbon of propene. The third isomer is a three-membered ring $Ce(CH_2CHCH_3)$ (C_1) with Ce addition to the two vinylic carbons [Fig. 4(c)], which is ~0.51 eV above the insertion isomer. All three isomers have a triplet ground state with the valence electron configuration of Ce $4f^1 6s^1$. Ionization removes the Ce $6s^1$ electron and yields a doublet ion. A bare Ce atom has the ground electron configuration $4f^1 5d^1 6s^2$. In forming these isomers, a Ce 6s electron in the ground electron configuration $4f^1 5d^1 6s^2$ is promoted to a Ce 5d orbital to form a low-energy $4f^1 5d^2 6s^1$ configuration to reduce the electron repulsion between the Ce $6s^2$ electrons and the electron cloud of the incoming ligand. The remaining two electrons that are associated with the $4f^1 5d^2 6s^1$ configuration of the isolated Ce atom are spin paired with one or two ligand orbitals. For example, in the inserted species $H—Ce(CH_2CHCH_2)$, the two electrons are in two 5 d orbitals, with one pairing up with the H $1s^1$ electron and other with the delocalized π^1 electron of the CH_2CHCH_2 radical [Fig. 5(a)].

To investigate the possible contributions from ionization of these isomers, we first compare the computed IEs and simulated spectra of all three isomers with the experimental spectra. The DFT predicted IEs (i.e., 0–0 transition energies) are 42 417 cm^{-1}, 41718 cm^{-1}, and 40 934 cm^{-1} (5.26 eV, 5.17 eV, and 5.08 eV) for $H—Ce(CH_2CHCH_2)$, $Ce(CH_2CH_2CH_2)$, and $Ce(CH_2CHCH_3)$, respectively. Compared to the experimental IE at 41 868 cm^{-1} (5.191 eV), the calculated IEs of the three isomers are all within the DFT computational uncertainties, which are typically on the order of a fraction of eV for open-shell organometallic species. Therefore, the theoretical IEs could not be used to differentiate the three isomers. Figures 2(b)–2(d) display the simulated spectra for the transitions from the triplet ground state of the neutral molecule to the doublet state of the ion of the three isomers at 200 K. In these simulations, the calculated 0–0 transition energy of each isomer is aligned with the strongest band at 41 868 cm^{-1}, but the theoretical vibrational frequencies are not scaled for the sake of clear comparison. The simulation of $H—Ce(CH_2CHCH_2)$ [Fig. 2(b)] displays a progression of 266 cm^{-1} and a hot band at 237 cm^{-1}, which compares well to the measured 272 cm^{-1} and 240 cm^{-1} intervals, though the intensity of the 272 cm^{-1} progression is somewhat overestimated. The simulation of $Ce(CH_2CH_2CH_2)$ [Fig. 2(c)] exhibits a very weak 0–0 band and a long FC spectral profile from a strongly active 135 cm^{-1} ion mode and modestly active 324 cm^{-1} and 528 cm^{-1} ion modes and thus does not mirror the observed spectrum at all. The simulation of $Ce(CH_2CHCH_3)$ [Fig. 2(d)] displays 197 cm^{-1} and 266 cm^{-1} progression above the 0–0 transition and two hot bands corresponding to the first and second quantum transitions of a neutral vibrational mode at 101 cm^{-1}. Although the separation (69 cm^{-1}) of the 197 cm^{-1} and 266 cm^{-1} progressions matches with the separation (65 cm^{-1}) of the observed two band systems, the frequency of the active neutral mode (101 cm^{-1}) is less than one half of the measured frequency (240 cm^{-1}), and the predicted hot-band intensity is too high. The intensity of the hot band would be reduced by decreasing the simulation temperature. However, simulations at lower temperatures did not reproduce the observed sequence bands on the higher energy side of the 272 cm^{-1} progression. Therefore, only the simulation of the inserted species is in good agreement with the 41 868 cm^{-1} band systems in the MATI spectrum. The measured energy and intensity of each band in the 41 868 cm^{-1} band system are listed in Table S3, along with those from the DFT and multidimensional FC calculations. The 272 cm^{-1} progression and 240 cm^{-1} band are assigned to a largely Ce—H bond wag in the ionic and neutral species, respectively, while the 330 cm^{-1} band is attributed to another Ce—H bond wag (Table I). Both of the Ce—H wags are coupled with the wagging motions of the CH_2CHCH_2 moiety. The difference between the two modes is that the wagging motions of the CH_2CHCH_2 moiety are in opposite directions. The activity of the Ce—H wag mode is due to a large change of the C2—Ce—H angle upon ionization (~9.8, Table S1). The 32 cm^{-1} shoulders are sequence bands due to the transitions from the first vibrational level of the 240 cm^{-1} mode in the neutral molecule to the vibrational levels of the 270 cm^{-1} mode in the ion. It should be noted that the MATI spectrum of $La(C_3H_6)$ formed in the La + propene reaction was also attributed to the ionization of the inserted species $H—La(CH_2CHCH_2)$, but the spectrum of $La(C_3H_6)$ exhibits only a single band system.[71]

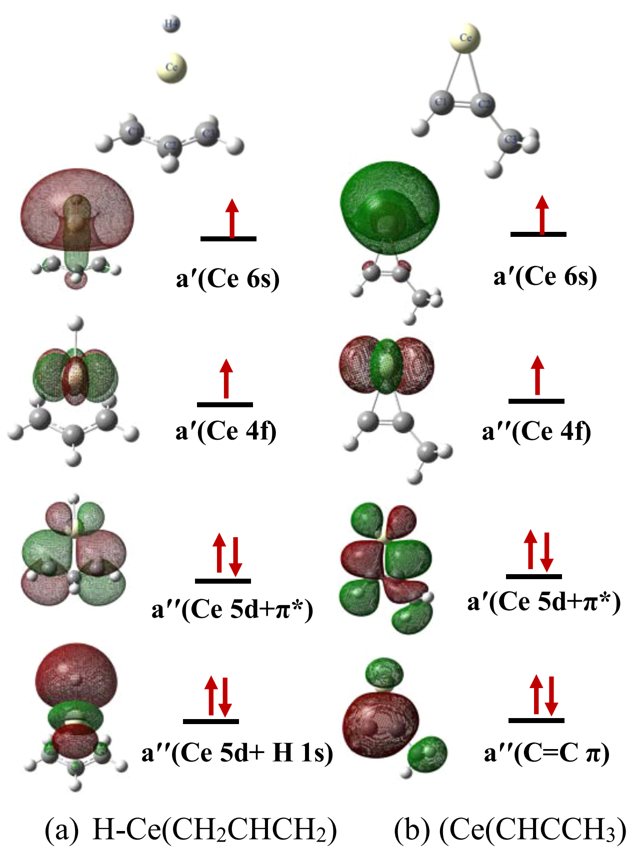

FIG. 5. Four lowest-energy valence molecular orbitals of (a) $H—Ce(CH_2CHCH_2)$ (C_s) and (b) $Ce(CHCCH_3)$ (C_s) with electron occupation for each orbital.

$Ce(C_3H_4)$: $Ce(C_3H_4)$ is formed by dehydrogenation of propene. Dehydrogenation could occur from any of the three carbon atoms and produces various isomers. Figures 4(d) and 4(e) present two lowest-energy isomers: $Ce(CHCHCH_2)$ (C_1), a four-membered metallocycle formed by 1,3- or 3,3-dehydrogenation,

TABLE I. Energies (cm^{-1}) of the origin bands and vibrational frequencies (cm^{-1}) of H—Ce(CH_2CHCH_2) (C_s) and Ce($CHCCH_3$) (C_s) from MATI spectra and theoretical calculations.

Molecule	MATI[a]	Theory[b]	Mode description[c]
H—Ce(CH_2CHCH_2)			
Origin bands	41 868/41 803	41 489/41 456	
ν_{13}^+ (a′)	330	343	Ce—H bond wag
ν_{14}^+/ν_{14} (a′)	272/240	266/237	Ce—H bond wag
Ce($CHCCH_3$)			
Origin bands	41 035/40 909	39 850/39 727	
ν_{10}^+ (a′)	557	570	Ce—C1 stretch and C1—H in-plane bend
ν_{11}^+ (a′)	440	445	Ce—C2 stretch and C2—CH_3 in-plane bend
ν_{12}^+ (a′)	205	222	C2—CH_3 in-plane bend

[a]The uncertainty for the AIEs are ~10 cm^{-1}.
[b]Energies of the origin bands are from the SOC-MCQDPT calculations with vibrational zero-point corrections from the DFT/B3LYP calculations. The two origin bands of H—Ce(CH_2CHCH_2) (C_s) refer to the $1^2E_{1/2} \leftarrow 1A'/2A'$ and $1^2E_{1/2} \leftarrow 1A''/2A''$ (S ≈ 1) SOC electronic transitions, while the two origin bands of Ce($CHCCH_3$) (C_s) refer to the $1^2E_{1/2} \leftarrow 1A''/2A''$ (S ≈ 1) and $1^2E_{1/2} \leftarrow 1A'/2A'$ SOC electronic transitions. The vibrational frequencies are calculated from DFT/B3LYP for the $^2A'$ ionic and $^3A'$ neutral R–S states of each species.
[c]The two Ce—H wagging modes are coupled with wagging motions of the CH_2CHCH_2 moiety in opposite directions.

and Ce($CHCCH_3$) (C_s), a three-membered ring formed by 1,2-dehydrogenation. Ce($CHCCH_3$) is at slightly higher energy (995 cm^{-1} or 0.123 eV) than Ce($CHCHCH_2$). Like Ce(C_3H_6), both Ce(C_3H_4) isomers have a triplet ground electronic state with the Ce $4f^1 6s^1$ configuration in the neutral molecule and a doublet state with the Ce $4f^1$ configuration in the ion. The valence orbitals of the neutral Ce($CHCCH_3$) are presented in Fig. 5(b), which include the Ce $4f^1$- and $6s^1$-based orbitals, a spin-paired molecular orbital that is bonding combination between Ce $5d_\pi$ and hydrocarbon π^* orbitals, and a C=C π orbital. The IEs are predicted to be 41 912 cm^{-1} (5.196 eV) for Ce($CHCHCH_2$) and 41 622 cm^{-1} (5.160 eV) for Ce($CHCCH_3$), and both are comparable to the energy of the strongest band origin (41 035 cm^{-1} or 5.088 eV) in the MATI spectrum [Fig. 3(a)]. The simulation of the Ce($CHCHCH_2$) $^2A \leftarrow {}^3A$ transition [Fig. 3(b)] displays the strongest activity for an ion mode of 113 cm^{-1} and the modest activity for three other ion modes of 281 cm^{-1}, 374 cm^{-1}, and 642 cm^{-1}, and it is not consistent with the observation of 205 cm^{-1}, 440 cm^{-1}, and 557 cm^{-1} vibronic bands. On the other hand, the simulation of the Ce($CHCCH_3$) $^2A' \leftarrow {}^3A'$ transition shows three active ion modes at 222 cm^{-1}, 445 cm^{-1}, and 570 cm^{-1}, which are in very good agreement with the three observed vibronic bands (205 cm^{-1}, 440 cm^{-1}, and 557 cm^{-1}) of the 41 035 cm^{-1} band system. Table S4 lists the measured energy and intensity of each band of the 41 035 cm^{-1} band system in comparison with those from the theoretical calculations. By comparing the spectrum and the simulation of Ce($CHCCH_3$), the 205 cm^{-1} progression is assigned to the C2—CH_3 in-plane bend excitation, the 440 cm^{-1} progression to the Ce—C2 stretch in combination with a C2—CH_3 in-plane bend, and the 557 cm^{-1} progression to the Ce—C1 stretch in combination with a C1—H in-plane bend (Table I). All three are the vibrational modes of the ion. The stronger activities of the Ce—C2 and Ce—C1 stretching modes arise from the significant changes of the Ce—C1/C2 bond lengths (0.05–0.06 Å, Table S2) upon ionization. Although the simulation of the $^2A' \leftarrow {}^3A'$ transition of the Ce($CHCCH_3$) isomer successfully explains the observed three vibrational progressions in the 41 035 cm^{-1} band system, it fails to account for the 40 909 cm^{-1} band system and the 360 cm^{-1} band. These bands will be discussed in Sec. III D by including SOC.

The other isomer, Ce($CHCHCH_2$), is not observed by the MATI measurement even though it is predicted to be ~0.1 eV lower in energy than Ce($CHCCH_3$). A possible reason for the lack of the MATI spectrum of Ce($CHCHCH_2$) could be that the formation of this isomer is kinetically unfavorable. However, a computational search of Ce + C_3H_6 reaction pathways shows no positive reaction barrier along the reaction coordinates for the formation of both isomers (Fig. S1). A second possibility could be due to the unfavorable FC activity. However, its simulation displays appreciable FC activities [Fig. 3(b)]. Moreover, a MATI spectrum was previously observed for La($CHCHCH_2$).[71] Thus, we suspect that the energy ordering of the two Ce(C_3H_4) isomers was predicted incorrectly.

D. Spin–orbit coupling

Attempting to explain the second band system in the spectra of Ce(C_3H_6) and Ce(C_3H_4), we performed multiconfiguration computations without and with SOC at the MCSCF and MCQDPT levels. Because there are seven 4f orbitals in a Ce atom, the Ce $4f^1 6s^1$ configuration in the neutral states of both species could form seven triplets and seven singlets depending on the relative orientations of the $4f^1$ and $6s^1$ electrons, and the Ce $4f^1$ configuration in the ion could form seven doublet states. The symmetries of these electronic states are determined by the symmetries of the 4f orbitals, which are 4A′ and 3A′′ in C_s. Tables II and III list several lowest Russell–Sanders (R–S) and SOC terms of the neutral and ionic H—Ce(CH_2CHCH_2) and Ce($CHCCH_3$) species from these calculations. The SOC terms of the neutral molecules in the two tables are labeled with

TABLE II. Lowest Russell–Saunders (R–S) and SOC terms, and adiabatic ionization energies (AIEs)[a] of H—Ce(CH_2CHCH_2) (C_s) from the multiconfiguration calculations without and with SOC (all expressed in cm^{-1}).

	Without SOC				With SOC	
R–S term	MCSCF	MCQDPT	SOC-term	SOC-MCSCF	SOC-MCQDPT	R–S term contribution (%)[b]
H–Ce(CH_2CHCH_2)						
$1^1A'$	122	−126	$1A'$	0	0	44 $^3A'$, 44 $^1A'$, 6 $^3A''$
$2^1A'$	138	−86	$2A'$	3	0	44 $^3A'$, 46 $^1A'$, 5 $^3A''$
$1^3A'$	0	0	$1A''(S \approx 1)$	77	29	89 $^3A'$, 6 $^1A''$
$2^3A'$	15	50	$2A''(S \approx 1)$	79	36	88 $^3A'$, 6 $^3A''$, 3 $^1A''$
$1^3A''$	402	437	$3A''(S \approx 1)$	488	629	58 $^3A''$, 35 $^3A'$, 4 $^1A''$
$1^1A''$	716	513	$4A''(S \approx 1)$	542	642	50 $^3A''$, 40 $^3A'$, 6 $^1A''$
$2^3A''$	519	812	$3A'(S \approx 1)$	646	719	55 $^3A''$, 38 $^3A'$, 6 $^1A''$
[H—Ce(CH_2CHCH_2)]$^+$						
$1^2A'$	0	0	$1^2E_{1/2}$	0	0	87 $^2A'$, 10 $^2A''$
$2^2A'$	33	54				
$3^2A''$	361	345	$2^2E_{1/2}$	477	469	69 $^2A'$, 29 $^2A''$
$4^2A''$	474	483				
AIE	37 996	41 464		37 920	41 489	

[a]The AIEs include vibrational zero-point energy corrections from DFT/B3LYP calculations.
[b]R–S terms ≥2% from the SOC-MCQDPT calculations.

symmetries only because they are neither pure singlets nor triplets. If a SOC term contains ≥90% triplets, it is indicated with S ≈ 1. The SOC term symmetries are the direct products of the electron spatial and spin symmetries of the contributing R–S terms (listed in these tables) that yield non-zero SOC matrix elements or a totally symmetric representation.[51]

H—Ce(CH_2CHCH_2): The low-energy R–S terms (Table II) are in a very narrow energy window (<0.1 eV). The MCSCF calculations treat primarily static electron corrections and predict the lowest energy triplets ($1^3A'$ and $2^3A'$) to be slightly more stable than the lowest-energy singlets ($1^1A'$ and $2^1A'$) of the neutral species. The energy ordering of the triplets vs singlets is the same as that from the

TABLE III. Lowest Russell–Saunders (R–S) and SOC terms and adiabatic ionization energies (AIEs)[a] of Ce($CHCCH_3$) (C_s) from multiconfiguration calculations without and with SOC (all expressed in cm^{-1}).

	Without SOC				With SOC	
R–S term	MCSCF	MCQDPT	SOC-term	SOC-MCSCF	SOC-MCQDPT	R–S term contribution %[b]
Ce($CHCCH_3$)						
$1^3A'$	0	0	$1A''(S \approx 1)$	0	0	91 $^3A'$, 6 $^3A''$, 3 $^1A''$
$2^3A'$	10	3	$2A''(S \approx 1)$	6	4	91 $^3A'$, 7 $^3A''$, 2 $^1A''$
$1^1A'$	549	331	$1A'$	206	127	52 $^3A'$, 37 $^1A'$, 8 $^3A''$
$2^1A'$	559	342	$2A'$	210	131	52 $^3A'$, 37 $^1A'$, 8 $^3A''$
$1^3A''$	676	582	$3A'/A''(S \approx 1)$	727	646	98 $^3A''$
$2^3A''$	710	599	$4A''$	849	723	73 $^3A''$, 24 $^1A''$
$1^1A''$	1132	875	$4A'$	880	800	81 $^3A''$, 14 $^1A''$
[Ce($CHCCH_3$)]$^+$						
$1^2A'$	0	0	$1^2E_{1/2}$	0	0	90 $^2A'$, 10 $^2A''$
$2^2A'$	33	54				
$1^2A''$	361	345	$2^2E_{1/2}$	537	484	71$^2A'$, 28 $^2A''$
$2^2A''$	474	483				
AIE	37 253	39 870		37 218	39 856	

[a]The AIEs include vibrational zero-point energy corrections from DFT/B3LYP calculations.
[b]R–S terms ≥2% from the SOC-MCQDPT calculations.

DFT calculations. Adding dynamic electron correlations to MCSCF by MCQDPT switches the energy ordering of the lowest-energy triplets and singlets but does not change the ordering of the other lower-energy states ($1^3A''$, $1^1A''$, and $2^3A''$). For the ionic species, both MCSCF and MCQDPT methods yield similar results. The small energy differences (~100 cm^{-1}) between the $1^1A'/2^1A'$ singlets and the $1^3A'/2^3A'$ triplets suggest the potential mixing of the singlet and triplet spin states. We thus performed additional calculations by including SOC. Indeed, both SOC-MCSCF and SOC-MCQDPT calculations (Table II) predict strong interactions between the $^1A'$ and $^3A'$ states. At the MCQDPT level, the two lowest, nearly degenerate SOC terms 1A′ and 2A′ consist of 44% $^3A'$ and 44% $^1A'$ S–R terms. The next nearly degenerate pair (1A″/2A″, S ≈ 1) is made of largely $^3A'$ S–R terms and is located at 76 cm^{-1} with SOC-MCSCF or 33 cm^{-1} with SOC-MCQDPT above the 1A′/2 A′ states. Other SOC terms are made of largely $^3A'$ and $^3A''$ S–R terms and are at considerably higher energies (≥~500 cm^{-1}). For the ionic species, the lowest SOC state is a degenerate state $1^2E_{1/2}$, which is followed by another degenerate state $2^2E_{1/2}$ at ~500 cm^{-1}. By comparing the multiple configuration calculations and splitting of the two band systems, the most likely assignment for the observed two band systems is that they arise from the $1^2E_{1/2} \leftarrow 1A'/2A'$ and $1^2E_{1/2} \leftarrow 1\ A''/2A''$ (S ≈ 1) transitions of the inserted isomer. This assignment gives the computational splitting of 76 cm^{-1} at the SOC-MCSCF level and 33 cm^{-1} at the SOC-MCQDPT level. Both theoretical values are in fair agreement with the measured value of 65 cm^{-1}, though it is interesting to note that the computation without dynamic electron correlation treatment seems to be slightly better in this case. With the SOC assignment, we can then refine spectral simulations by including both transitions. To do so, we use the $1^3A'$ S–R term to represent the initial neutral states and the $1^2A'$ S–R term to represent the final ion state because the SOC levels are made of the $^3A'$ and $^2A'$ S–R terms, respectively. The combined simulation of the two SOC transitions [Fig. 2(e)] clearly accounts for the observed two band systems [Fig. 2(a)].

Ce(CHCCH$_3$): The MCSCF and MCQDPT calculations without and with SOC yield the same sequences for the low-lying energy states, and the dynamic electron correction treatment by MCQDPT improves the energy calculations (as it brings energy down) for the S–R and SOC terms (Table III). Without SOC, the first two pairs of nearly degenerate $1^3A'/2^3A'$ triplets and nearly degenerate $1^1A'/2^1A'$ singlets are separated by 549 cm^{-1} at the MCSCF level and 335 cm^{-1} at the MCQDPT level, respectively. The theoretical separations are about 3–5 times larger than the 126 cm^{-1} splitting observed in the MATI spectrum [Fig. 3(a)]. With SOC, the separation between the nearly degenerate 1A″/2A″ (S ≈ 1) states and the nearly degenerate 1A′/2A′ states is calculated to be ~200 cm^{-1} with SOC-MCSCF and ~130 cm^{-1} with SOC-MCQDPT, respectively. The computed energy separations by both methods are in reasonable agreement with the measured splitting of 126 cm^{-1}. Particularly, the value predicted by SOC-MCQDPT is almost identical to the experimental value. The SOC terms 1A″/2A″ contain mostly a $^3A'$ S–R term, while the next twin SOC terms consist of heavily mixed triplet and singlet S–R states. The reasonable match between the predicted and measured splittings suggests that the observed two band systems in the MATI spectrum likely arise from the $1^2E_{1/2} \leftarrow 1A''/2A''$ and $1^2E_{1/2} \leftarrow 1A'/2A'$ transitions. The combined simulation from these two transitions by using the $1^3A'$ S–R state to represent for the initial SOC states and the $1^2A'$ for the final SOC states is shown in Fig. 3(d). Again, the calculated and measured spectra are in reasonable agreement. Transitions from other SOC terms (e.g., 3A′/3A″, 4A″, and 4A′) of the neutral molecule are not expected because they are at considerably higher energies and would not be significantly populated under supersonic cooling conditions. The intensity ratio of the two origin bands $I_{40909}/I_{40135} \approx 0.4$ from which the electronic temperature is estimated to be ~200 K. At this temperature, the population of the 3A′/3A″ at 646 cm^{-1} from the SOC-MCQDPT calculations is only about 1%. The transition at 360 cm^{-1} to the blue of the 41 035 cm^{-1} origin band could be associated with the $2^2E_{1/2}$ – 1A″/2A″ transitions. The $2^2E_{1/2}$ ion state is predicted to be higher than the lowest ion state $1^2E_{1/2}$ by 537 cm^{-1} at the SOC-MCSCF level and by 484 cm^{-1} at the SOC-MCQDPT level. However, because no other vibronic bands are observed, this assignment can only be tentative.

The separations between the two pairs of the lowest SOC terms of the neutral molecules are measured to be significantly different between H—Ce(CH$_2$CHCH$_2$) (65 cm^{-1}) and Ce(CHCCH$_3$) (126 cm^{-1}) although the two molecules have the same ground valence electron configuration Ce $4f^16s^1$. The SOC variation is associated with molecular shapes where SOC is modified from the usual spherical symmetry of the atom and couples the electron spin to current running around the molecule.[88] Although both H—Ce(CH$_2$CHCH$_2$) and Ce(CHCCH$_3$) are in C_s symmetry, their shapes are different as Ce inserting into an allylic C—H bond of the methyl group in H—Ce(CH$_2$CHCH$_2$) while Ce coordinating to the two vinylic carbon atoms in Ce(CHCCH$_3$). The SOC dependence on the molecule shape has also been observed previously for the two isomers of Ce(C$_4$H$_6$) formed in the Ce + alkene reactions, where the tetrahedron-like C_{3v} isomer exhibits two SOC vibronic band systems separated by 88 cm^{-1}, while the five-membered metallocyclic C_s isomer displays three SOC terms split by 60 cm^{-1} and 101 cm^{-1}.[52] On the other hand, the three-membered cyclic Ce(CHCCH$_3$) observed in this work shows almost identical separation between the two pairs of the lowest SOC terms (126 cm^{-1}) to that of the three-membered cyclic Ce(C$_2$H$_2$) (128 cm^{-1}) formed in the Ce + ethylene reaction.[50] In these two molecules, a hydrogen atom in Ce(C$_2$H$_2$) is replaced by a methyl group in Ce(CHCCH$_3$).

IV. CONCLUSIONS

The Ce atom reaction with propene produces several Ce–hydrocarbon complexes through Ce insertion, dehydrogenation, and carbon–carbon cleavage and coupling. Ce(C$_3$H$_6$) and Ce(C$_3$H$_4$) are probed by MATI spectroscopy. The spectrum of each species consists of two band systems, each with several vibronic bands. Ce(C$_3$H$_6$) is identified by combining the measured spectra with theoretical calculations as an inserted species H—Ce(CH$_2$CHCH$_2$) and Ce(C$_3$H$_4$) as a dehydrogenation cyclic species Ce(CHCCH$_3$). Both species have the Ce $4f^16s^1$ ground electron configuration and a C_s symmetry with different shapes. Ionization of each species by removing the Ce 6s electron yields the ionic species with the Ce $4f^1$ configuration. The multiconfiguration calculations without involving SOC predict the lowest-energy states of the neutral molecules to be a pair of nearly degenerate triplet states and a pair of nearly degenerate singlet states. The triplet and singlet states are predicted to be coupled with each other by the relativistic computations. The observed two band systems are attributed to the transitions from the two pairs of the lowest SOC neutral states to the lowest-energy doubly degenerate doublet ionic state.

SUPPLEMENTARY MATERIAL

See the supplementary material for the geometries of three $Ce(C_3H_6)$ isomers and two $Ce(C_3H_4)$ isomers in the neutral and ionic states, experimental and calculated relative band energies and intensities, and reaction pathways for the formation of the $Ce(C_3H_4)$ two isomers from DFT/B3LYP calculations.

ACKNOWLEDGMENTS

We are grateful for the financial support from the National Science Foundation, Division of Chemistry (Chemical Structure, Dynamics, and Mechanisms; Grant No. 1800316).

REFERENCES

[1] V. Galitski and I. B. Spielman, Nature **494**, 49 (2013).
[2] O. Bolton, K. Lee, H.-J. Kim, K. Y. Lin, and J. Kim, Nat. Chem. **3**, 205 (2011).
[3] H. Li, A. Kamasah, S. Matsika, and A. G. Suits, Nat. Chem. **11**, 123 (2019).
[4] T. Penfold, E. Gindensperger, C. Daniel, and C. M. Marian, Chem. Rev. **118**, 6975 (2018).
[5] R. Ahuja, A. Blomqvist, P. Larsson, P. Pyykko, and P. Zaleski-Ejgierd, Phys. Rev. Lett. **106**, 018301 (2011).
[6] K. Goushi, K. Yoshida, K. Sato, and C. Adachi, Nat. Chem. **6**, 253 (2012).
[7] J. Zhao, W. Wu, J. Sun, and S. Guo, Chem. Soc. Rev. **42**, 5323 (2013).
[8] A. Kamkaew, S. H. Lim, H. B. Lee, L. V. Kiew, L. Y. Chung, and K. Burgess, Chem. Soc. Rev. **42**, 77 (2013).
[9] P. B. Armentrout, Chem. Eur. J. **23**, 10 (2017).
[10] J. Roithova and D. Schroeder, Chem. Rev. **110**, 1170 (2010).
[11] H. Schwarz, Angew. Chem., Int. Ed. **50**, 10096 (2011).
[12] P. G.-N. H. Schwarz, J. Li, M. Schlangen, X. Sun, T. Weiske, and S. Zhou, Organometallics **36**, 8 (2016).
[13] P. Schwach, X. Pan, and X. Bao, Chem. Rev. **117**, 8497 (2017).
[14] H. Schwarz, S. Shaik, and J. Li, J. Am. Chem. Soc. **139**, 17201 (2017).
[15] Y.-X. Zhao, Z.-Y. Li, Y. Yang, and S.-G. He, Acc. Chem. Res. **51**, 2603 (2018).
[16] T. B. Demissie, B. D. Garabato, K. Ruud, and P. M. Kozlowski, Angew. Chem., Int. Ed. **55**, 11503 (2016).
[17] S. Knecht, J. J. A. Jensen, and T. Saue, Nat. Chem. **11**, 40 (2019).
[18] L. Gagliardi and B. O. Roos, Nature **433**, 848 (2005).
[19] Y.-L. Wang, H.-S. Hu, W.-L. Li, F. Wei, and J. Li, J. Am. Chem. Soc. **138**, 1126 (2016).
[20] C. Peterson, D. A. Penchoff, and A. K. Wilson, J. Chem. Phys. **143**, 194109 (2015).
[21] G. Schoendorff, B. Chi, H. Ajieren, and A. K. Wilson, J. Phys. Chem. A **119**, 1683 (2014).
[22] G. Schoendorff, C. South, and A. K. Wilson, J. Phys. Chem. A **117**, 10881 (2013).
[23] C. South, G. Schoendorff, and A. K. Wilson, Int. J. Quant. Chem. **116**, 791 (2016).
[24] X. Cao and M. Dolg, Mol. Phys. **101**, 1967 (2003).
[25] O. Mooβen and M. Dolg, J. Phys. Chem. A **120**, 3966 (2016).
[26] M. Dolg and P. Fulde, Chem. Eur. J. **4**, 200 (1998).
[27] W. Liu, M. Dolg, and L. Li, J. Chem. Phys. **108**, 2886 (1998).
[28] M. Dolg, W. Liu, and S. Kalvoda, Int. J. Quantum Chem. **76**, 359 (2000).
[29] H. Moriyama, Y. Watanabe, H. Nakano, S. Yamamoto, and H. Tatewaki, J. Chem. Phys. **132**, 124310 (2010).
[30] G. Hong, M. Dolg, and L. Li, Int. J. Quantum Chem. **80**, 201 (2000).
[31] M. Hülsen, A. Weigand, and M. Dolg, Theor. Chem. Acc.: Theory, Comput., Model. (Theor. Chim. Acta) **122**, 23 (2009).
[32] J. Paulovic, L. Gagliardi, J. M. Dyke, and K. Hirao, J. Chem. Phys. **120**, 9998 (2004).
[33] B. O. Roos, R. Lindh, P.-Å. Malmqvist, V. Veryazov, P.-O. Widmark, and A. C. Borin, J. Phys. Chem. A **112**, 11431 (2008).
[34] B. O. Roos and P. Pyykko, Chem. Eur. J. **16**, 270 (2010).
[35] T. K. Todorova, I. Infante, L. Gagliardi, and J. M. Dyke, J. Phys. Chem. A **112**, 7825 (2008).
[36] T. K. Todorova, I. Infante, L. Gagliardi, and J. M. Dyke, Int. J. Quantum Chem. **109**, 2068 (2009).
[37] Z. L. Cao, Z. D. Li, F. Wang, and W. J. Liu, Phys. Chem. Chem. Phys. **19**, 3713 (2017).
[38] M. Sekiya, T. Noro, and T. Koga, Theor. Chem. Acc. **131**, 1247 (2012).
[39] Y. Nakajima, J. Seino, and H. Nakai, J. Chem. Phys. **139**, 244107 (2013).
[40] D. G. Fedorov and J. P. Finley, Phys. Rev. A **64**, 042502 (2002).
[41] Z. T. Fang, K. S. Thanthiriwatte, D. A. Dixon, L. Andrews, and X. F. Wang, Inorg. Chem. **55**, 1702 (2016).
[42] Y. Gong, L. Andrews, M. Chen, and D. A. Dixon, J. Phys. Chem. A **115**, 14581 (2011).
[43] Y. Gong, X. Wang, L. Andrews, M. Chen, and D. A. Dixon, Organometallics **30**, 4443 (2011).
[44] T. Mikulas, M. Chen, D. A. Dixon, K. A. Peterson, Y. Gong, and L. Andrews, Inorg. Chem. **53**, 446 (2014).
[45] T. C. Mikulas, M. Chen, Z. Fang, K. A. Peterson, L. Andrews, and D. A. Dixon, J. Phys. Chem. A **120**, 793 (2016).
[46] T. Vent-Schmidt, Z. Fang, Z. Lee, D. Dixon, and S. Riedel, Chem. Eur. J. **22**, 2406 (2016).
[47] X. F. Wang, L. Andrews, Z. T. Fang, K. S. Thanthiriwatte, M. Y. Chen, and D. A. Dixon, J. Phys. Chem. A **121**, 1779 (2017).
[48] X. Wang, H.-G. Cho, L. Andrews, M. Chen, D. A. Dixon, H.-S. Hu, and J. Li, J. Phys. Chem. A **115**, 1913 (2011).
[49] W. Liu and Y. Xiao, Chem. Soc. Rev. **47**, 4481 (2018).
[50] Y. Zhang, M. W. Schmidt, S. Kumari, M. S. Gordon, and D.-S. Yang, J. Phys. Chem. A **120**, 6963 (2016).
[51] Y. Zhang, S. Nyambo, and D.-S. Yang, J. Chem. Phys. **149**, 234301 (2018).
[52] Y. Zhang, W. Cao, and D.-S. Yang, J. Chem. Phys. **151**, 124307 (2019).
[53] K. Eller and H. Schwarz, Chem. Rev. **91**, 1121 (1991).
[54] C. Heinemann, D. Schröder, and H. Schwarz, Chem. Ber. **127**, 1807 (1994).
[55] H. H. Cornehl, C. Heinemann, D. Schroeder, and H. Schwarz, Organometallics **14**, 992 (1995).
[56] J. Marcalo, M. Santos, A. P. de Matos, J. K. Gibson, and R. G. Haire, J. Phys. Chem. A **112**, 12647 (2008).
[57] R. H. Schultz and P. B. Armentrout, Organometallics **11**, 828 (1992).
[58] C. L. Haynes and P. B. Armentrout, Organometallics **13**, 3480 (1994).
[59] P. Mourgues, A. Ferhati, T. B. McMahon, and G. Ohanessian, Organometallics **16**, 210 (1997).
[60] V. Baranov, H. Becker, and D. K. Bohme, J. Phys. Chem. A **101**, 5137 (1997).
[61] P. B. Armentrout and Y.-M. Chen, J. Am. Soc. Mass. Spectrom. **10**, 821 (1999).
[62] D. Ritter, J. J. Carroll, and J. C. Weisshaar, J. Phys. Chem. **96**, 10636 (1992).
[63] J. J. Carroll, K. L. Haug, and J. C. Weisshaar, J. Am. Chem. Soc. **115**, 6962 (1993).
[64] J. C. Weisshaar, Acc. Chem. Res. **26**, 213 (1993).
[65] J. J. Carroll, K. L. Haug, J. C. Weisshaar, M. R. A. Blomberg, P. E. M. Siegbahn, and M. Svensson, J. Phys. Chem. **99**, 13955 (1995).
[66] Y. Wen, M. Porembski, T. A. Ferrett, and J. C. Weisshaar, J. Phys. Chem. A **102**, 8362 (1998).
[67] M. Porembski and J. C. Weisshaar, J. Phys. Chem. A **105**, 6655 (2001).
[68] R. Z. Hinrichs, J. J. Schroden, and H. F. Davis, J. Phys. Chem. A **107**, 9284 (2003).
[69] J. J. Schroden and H. F. Davis, in *Modern Trend in Chemical Dynamics Part II: Experiment and Theory*, Advanced Series in Physical Chemistry Vol 14, edited by X. Yang and K. Lium (World Scientific, Singapore, 2004), p. 215.
[70] D. Hewage, W. Cao, S. Kumari, R. Silva, T. H. Li, and D.-S. Yang, J. Chem. Phys. **146**, 184304 (2017).

[71] S. Kumari, W. Cao, D. Hewage, R. Silva, and D.-S. Yang, J. Chem. Phys. **146**, 074305 (2017).
[72] B. R. Sohnlein, S. Li, J. F. Fuller, and D.-S. Yang, J. Chem. Phys. **123**, 014318 (2005).
[73] M. A. Duncan, T. G. Dietz, and R. E. Smalley, J. Chem. Phys. **75**, 2118 (1981).
[74] M. J. Frish, G. W. Trucks, H. B. Schlegel, G. E. Scuseria, M. A. Robb, J. R. Cheeseman, G. Scalmani, V. Barone, B. Mennucci, G. A. Petersson, H. Nakatsuji, M. Caricato, X. Li, H. P. Hratchian, A. F. Izmaylov, J. Bloino, and G. Zheng, Gaussian 09, Revision A.01, Gaussian, Inc., Wallingford, CT, 2009.
[75] S. Li, "Threshold photoionization and ZEKE photoelectron spectroscopy of metal complexes," Ph.D. thesis, University of Kentucky, 2004.
[76] J. Seino and H. Nakai, J. Chem. Phys. **136**, 244102 (2012).
[77] M. Barysz and A. J. Sadlej, J. Chem. Phys. **116**, 2696 (2002).
[78] D. Kedziera and M. Barysz, J. Chem. Phys. **121**, 6719 (2004).
[79] T. Noro, M. Sekiya, and T. Koga, Theoret. Chem. Acc. **131**, 1124 (2012).
[80] P. Piecuch, J. R. Gour, and M. Włoch, Int. J. Quantum Chem. **109**, 3268 (2009).
[81] K. R. Glaesemann and M. W. Schmidt, J. Phys. Chem. A **114**, 8772 (2010).
[82] M. W. Schmidt and M. S. Gordon, Annu. Rev. Phys. Chem. **49**, 233 (1998).
[83] H. Nakano, J. Chem. Phys. **99**, 7983 (1993).
[84] D. G. Fedorov, S. Koseki, M. W. Schmidt, and M. S. Gordon, Int. Rev. Phys. Chem. **22**, 551 (2003).
[85] D. G. Fedorov and M. S. Gordon, J. Chem. Phys. **112**, 5611 (2000).
[86] M. W. Schmidt, K. K. Baldridge, J. A. Boatz, S. T. Elbert, M. S. Gordon, J. H. Jensen, S. Koseki, N. Matsunaga, K. A. Nguyen, S. Su, T. L. Windus, M. Dupuis, and J. A. Montgomery, J. Comput. Chem. **14**, 1347 (1993).
[87] D. R. Lide, *CRC Handbook of Chemistry and Physics*, 88th ed. (CRC, Boca Raton, FL, 2008).
[88] A. L. Khosla, A. C. Jacko, J. Merino, and B. J. Powell, Phys. Rev. B **95**, 115109 (2017).